Supplement of

Contribution of physical latent knowledge to the emulation of an atmospheric physics model: a study based on the LMDZ Atmospheric General Circulation Model

Ségolène Crossouard[1], Soulivanh Thao[1], Thomas Dubos[2], Masa Kageyama[1], Mathieu Vrac[1], and Yann Meurdesoif[1]

[1]Laboratoire des Sciences du Climat et de l'Environnement (LSCE-IPSL), CEA-CNRS-UVSQ-Université Paris-Saclay, 91190 Gif-sur-Yvette, France
[2]Laboratoire de Météorologie Dynamique (LMD-IPSL), Ecole Polytechnique, 91120 Palaiseau, France

Correspondence: Ségolène Crossouard (segolene.crossouard@lsce.ipsl.fr)

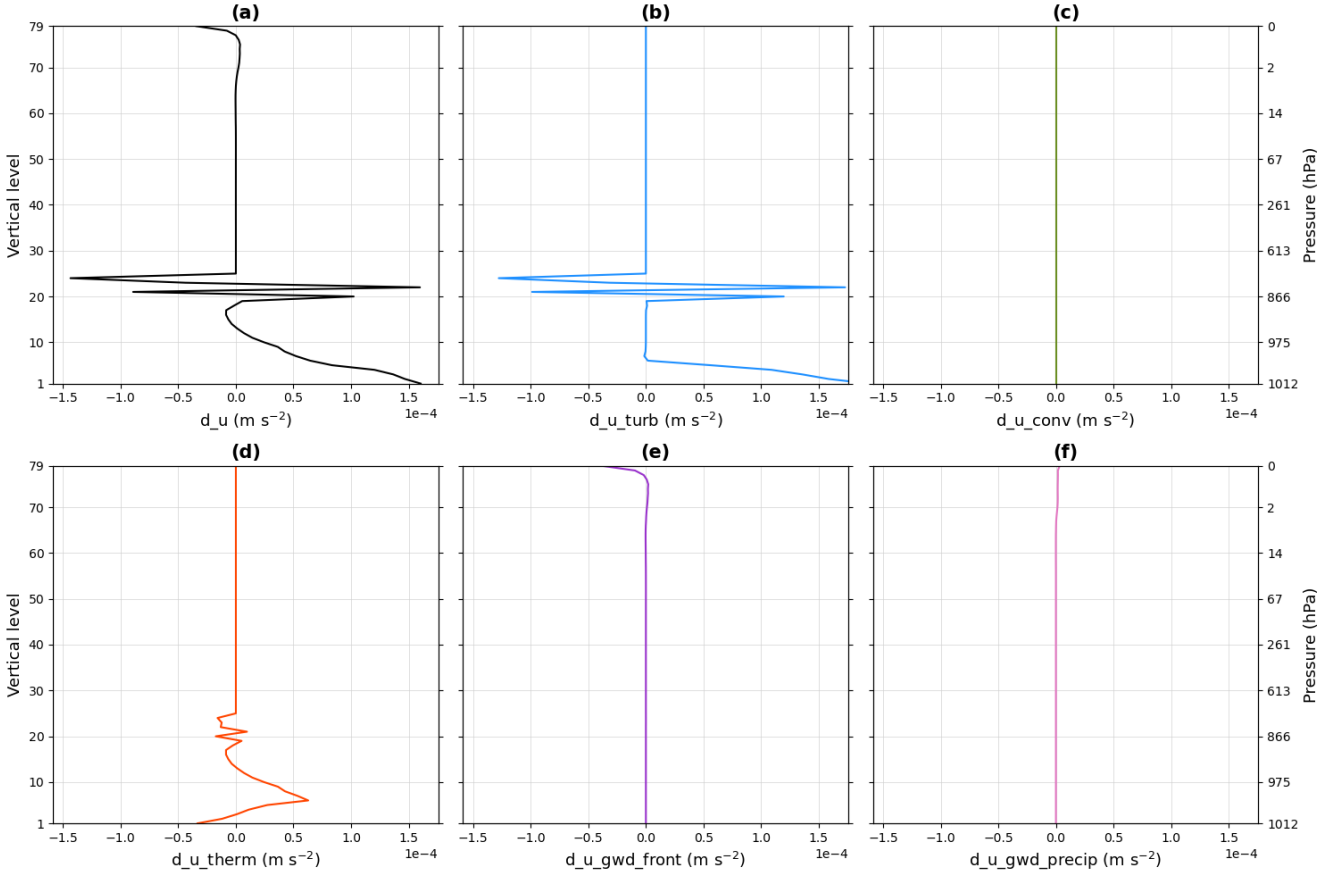

Figure S1. Vertical profile of the zonal wind tendency *d_u* **(a)** of the point A located in the high latitudes for one time step, and vertical profiles of the physical processes involved in the decomposition of this tendency: turbulence **(b)**, convection **(c)**, thermals **(d)**, gravity wave drags associated to fronts **(e)** and gravity wave drags associated to precipitations **(f)**.

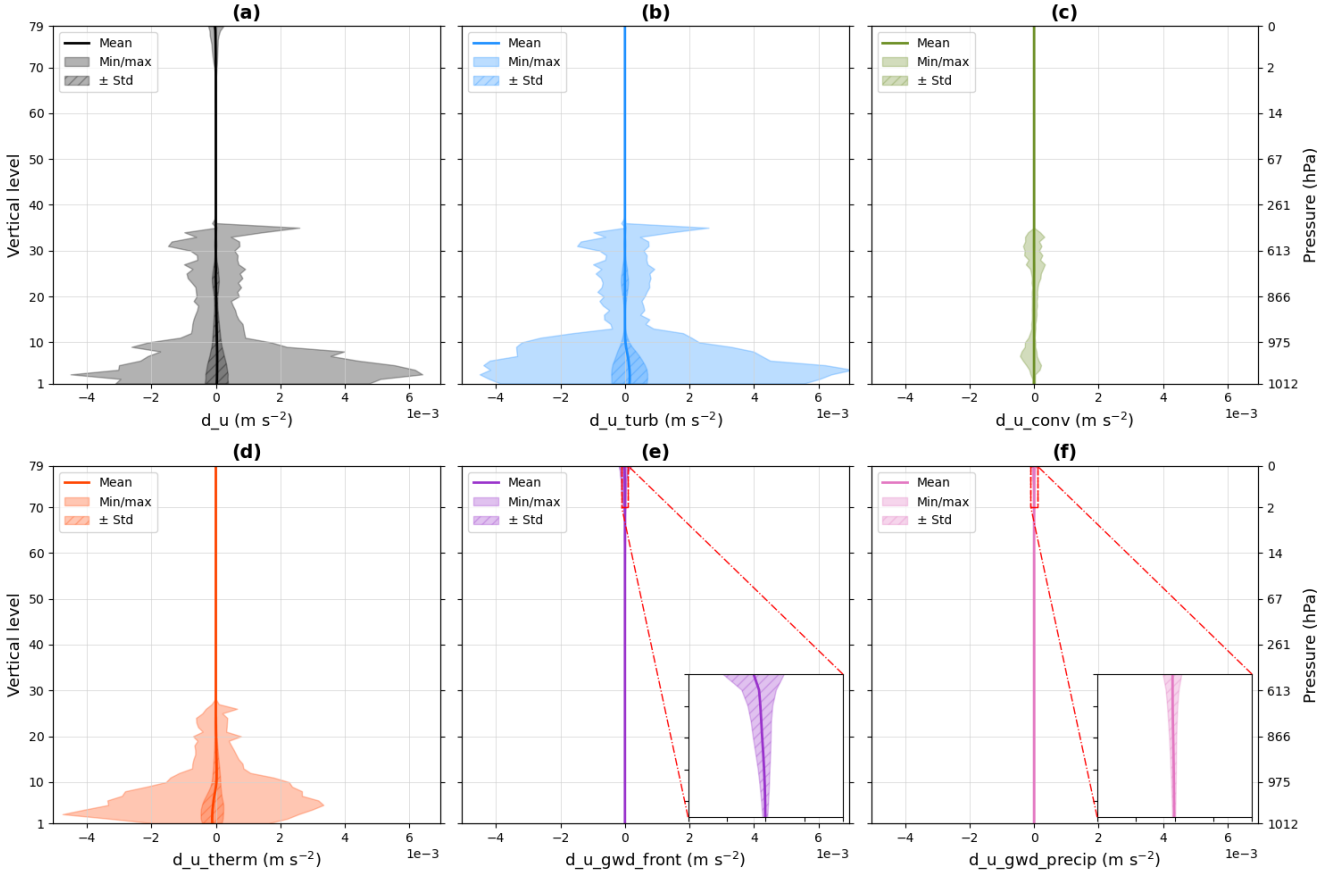

Figure S2. Mean vertical profile of the zonal wind tendency *d_u* **(a)** of the point A, located in the high latitudes, with minimum/maximum envelope and standard deviation bounds (hatched areas). The data used are from a full-year simulation. The same types of curves as the zonal wind tendency can be generated for the physical processes involved in the decomposition of this tendency: turbulence **(b)**, convection **(c)**, thermals **(d)**, gravity wave drags associated to fronts **(e)** and gravity wave drags associated to precipitations **(f)**.

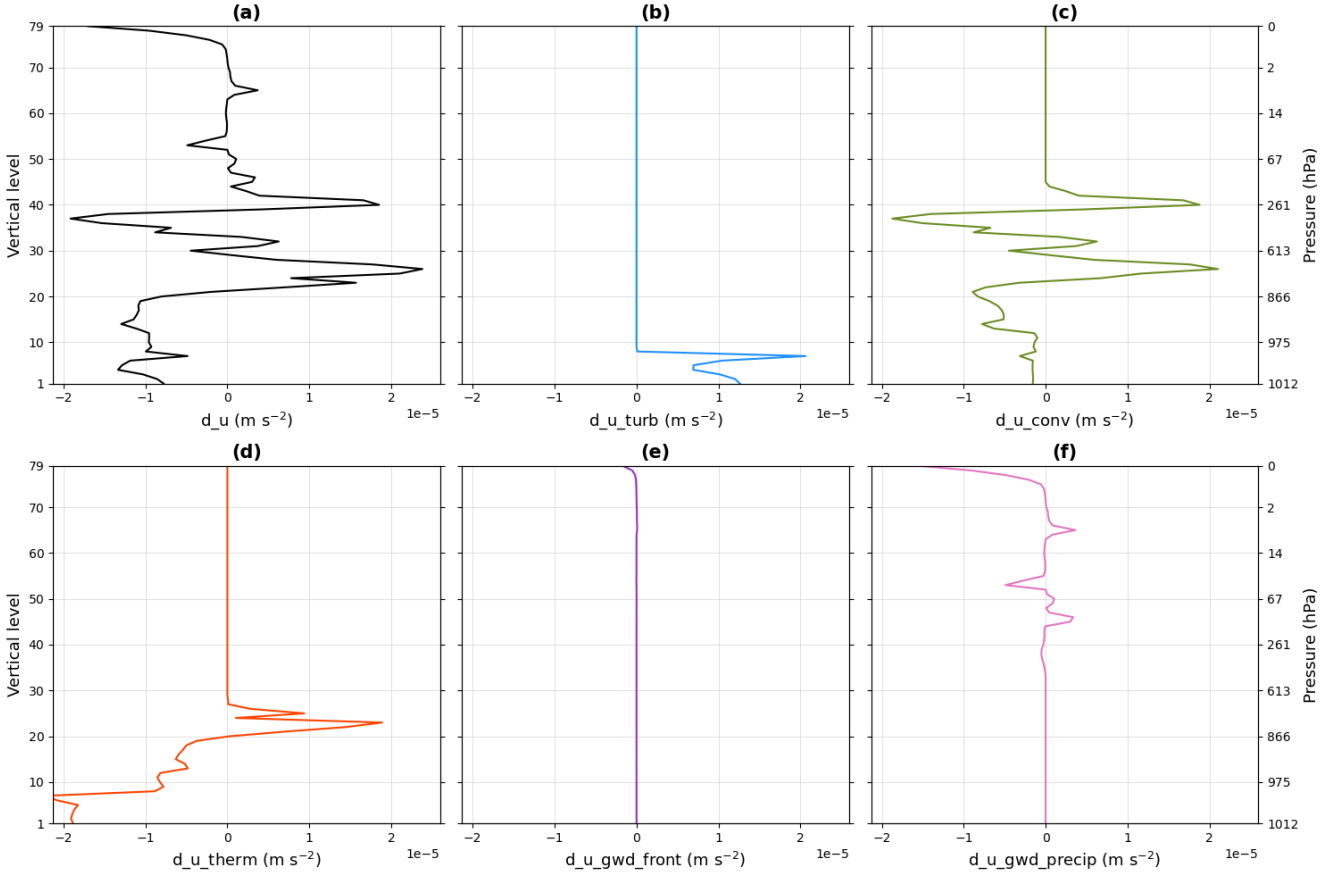

Figure S3. Vertical profile of the zonal wind tendency *d_u* **(a)** of the point C located near the equator for one time step, and vertical profiles of the physical processes involved in the decomposition of this tendency: turbulence **(b)**, convection **(c)**, thermals **(d)**, gravity wave drags associated to fronts **(e)** and gravity wave drags associated to precipitations **(f)**.

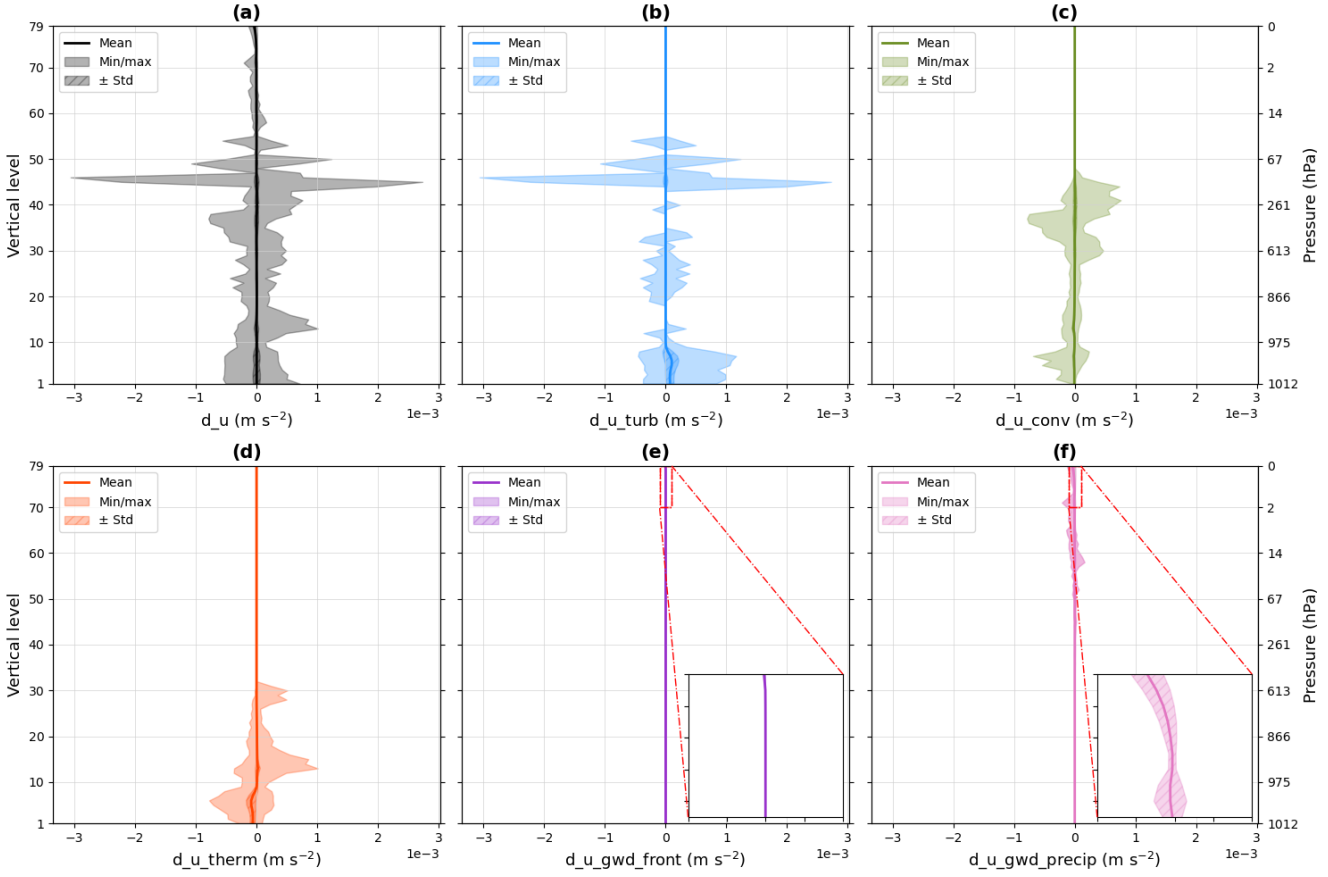

Figure S4. Mean vertical profile of the zonal wind tendency *d_u* **(a)** of the point C, located near the equator, with minimum/maximum envelope and standard deviation bounds (hatched areas). The data used are from a full-year simulation. The same types of curves as the zonal wind tendency can be generated for the physical processes involved in the decomposition of this tendency: turbulence **(b)**, convection **(c)**, thermals **(d)**, gravity wave drags associated to fronts **(e)** and gravity wave drags associated to precipitations **(f)**.

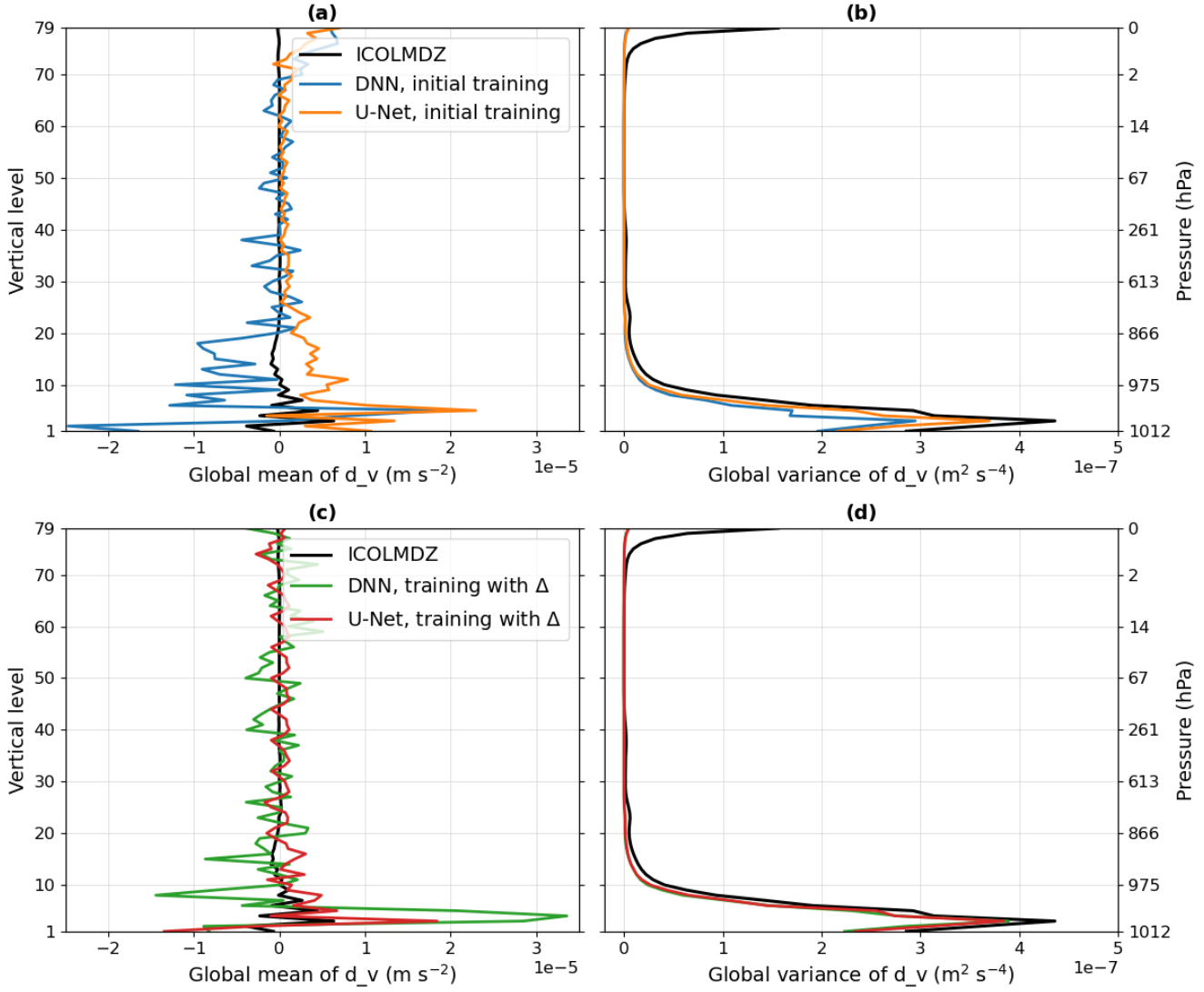

Figure S5. Global vertical profiles of the meridional wind tendency *d_v* of the mean (left) and the variance (right) for the test subset. Figures **(a)** and **(b)** show the results of the initial training, while figures **(c)** and **(d)** correspond to the second training where physical knowledge is added. In these figures, the black curves represent the real data from the ICOLMDZ simulation. The blue and green curves correspond to predictions made by DNNs while the orange and red curves represent the results obtained using U-Nets.

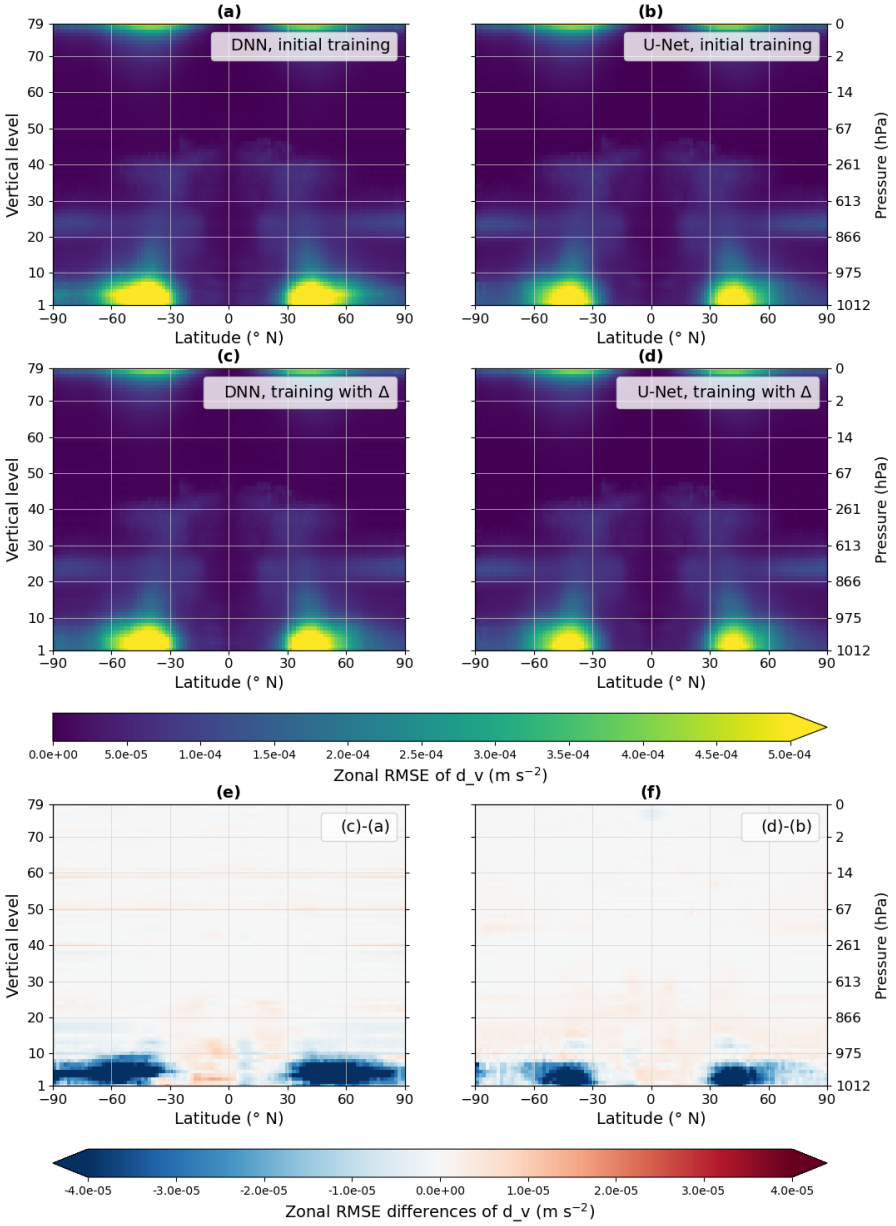

Figure S6. Cross-sections of the zonal RMSE of the meridional wind tendency *d_v* for the test subset. Figures **(a)** and **(b)** show the results from the DNN and the U-Net respectively, from the initial approach in both cases, whereas figures **(c)** and **(d)** are the results of the DNN and the U-Net, with laplacians. Figures **(e)** and **(f)** are respectively the zonal RMSE differences between DNN with laplacians **(c)** and DNN without them **(a)**, and U-Net with laplacians **(d)** and U-Net without them **(b)**.

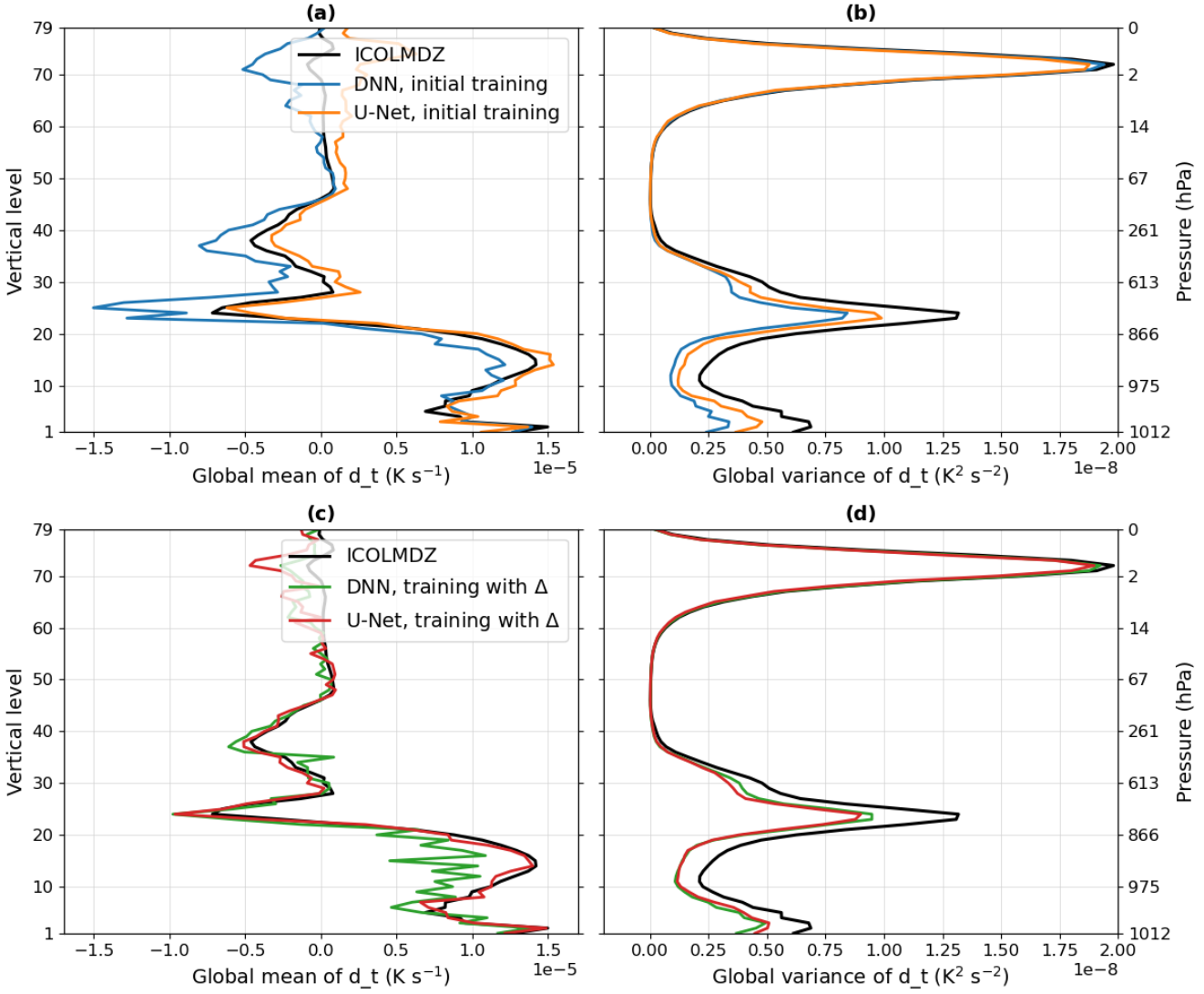

Figure S7. Global vertical profiles of the temperature tendency *d_t* of the mean (left) and the variance (right) for the test subset. Figures **(a)** and **(b)** show the results of the initial training, while figures **(c)** and **(d)** correspond to the second training where physical knowledge is added. In these figures, the black curves represent the real data from the ICOLMDZ simulation. The blue and green curves correspond to predictions made by DNNs while the orange and red curves represent the results obtained using U-Nets.

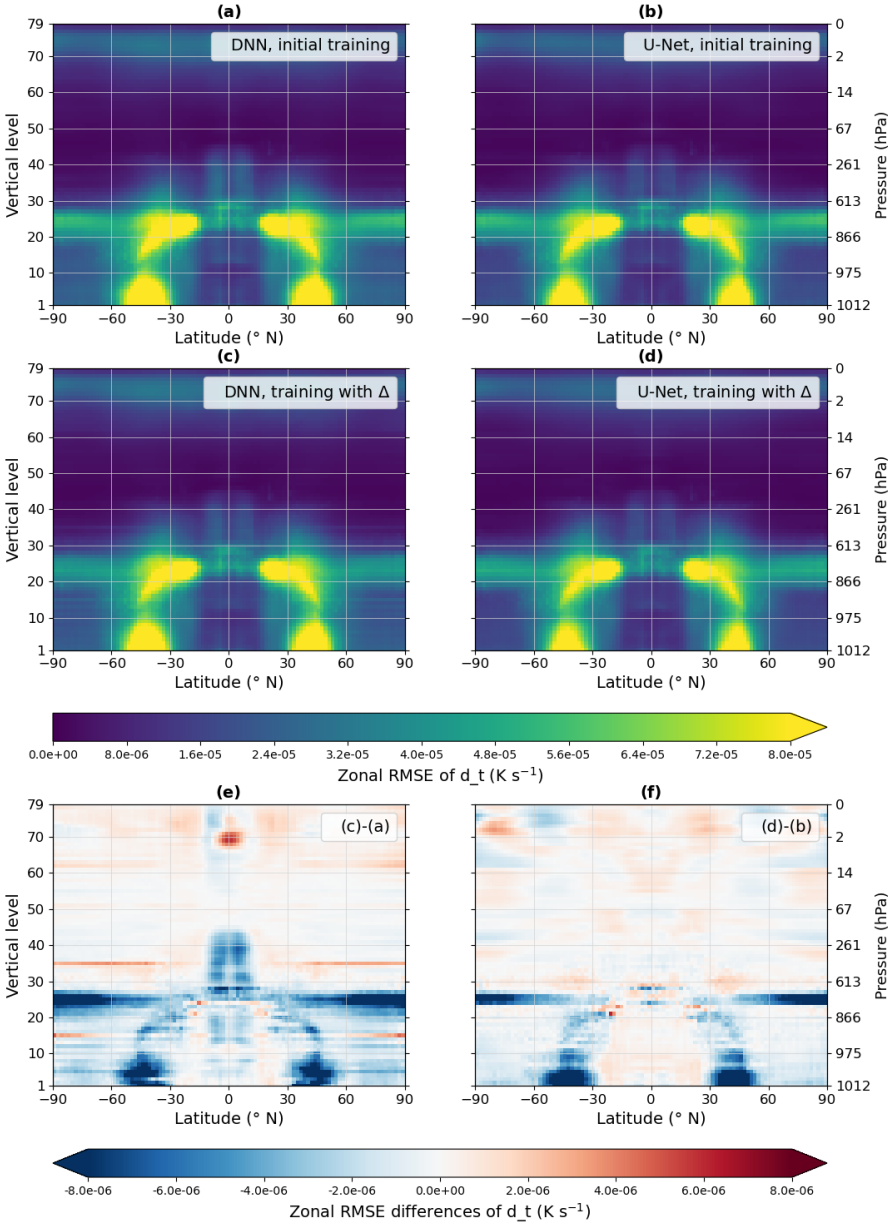

Figure S8. Cross-sections of the zonal RMSE of the temperature tendency *d_t* for the test subset. Figures **(a)** and **(b)** show the results from the DNN and the U-Net respectively, from the initial approach in both cases, whereas figures **(c)** and **(d)** are the results of the DNN and the U-Net, with laplacians. Figures **(e)** and **(f)** are respectively the zonal RMSE differences between DNN with laplacians **(c)** and DNN without them **(a)**, and U-Net with laplacians **(d)** and U-Net without them **(b)**.

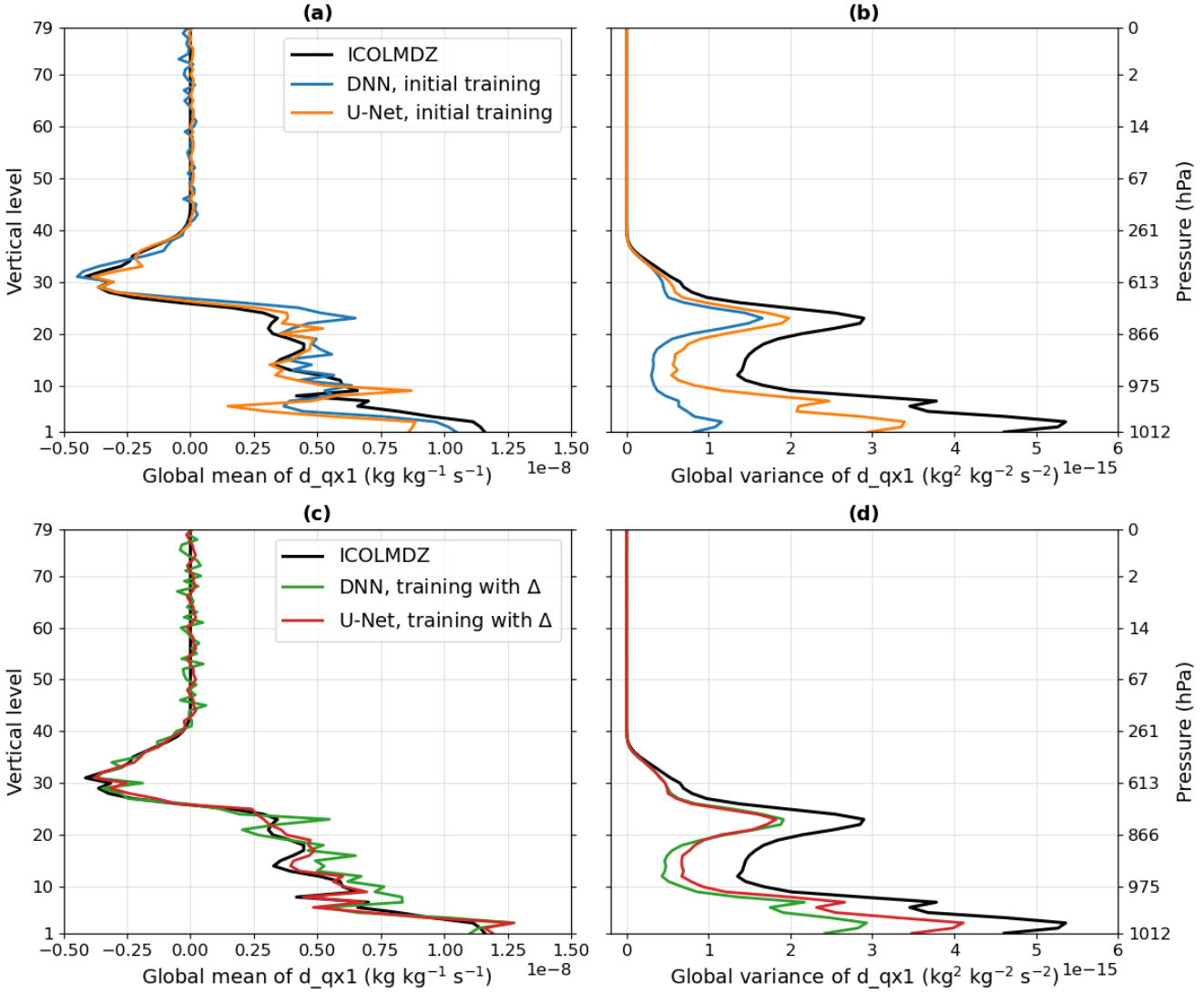

Figure S9. Global vertical profiles of the humidity tendency *d_qx1* of the mean (left) and the variance (right) for the test subset. Figures **(a)** and **(b)** show the results of the initial training, while figures **(c)** and **(d)** correspond to the second training where physical knowledge is added. In these figures, the black curves represent the real data from the ICOLMDZ simulation. The blue and green curves correspond to predictions made by DNNs while the orange and red curves represent the results obtained using U-Nets.

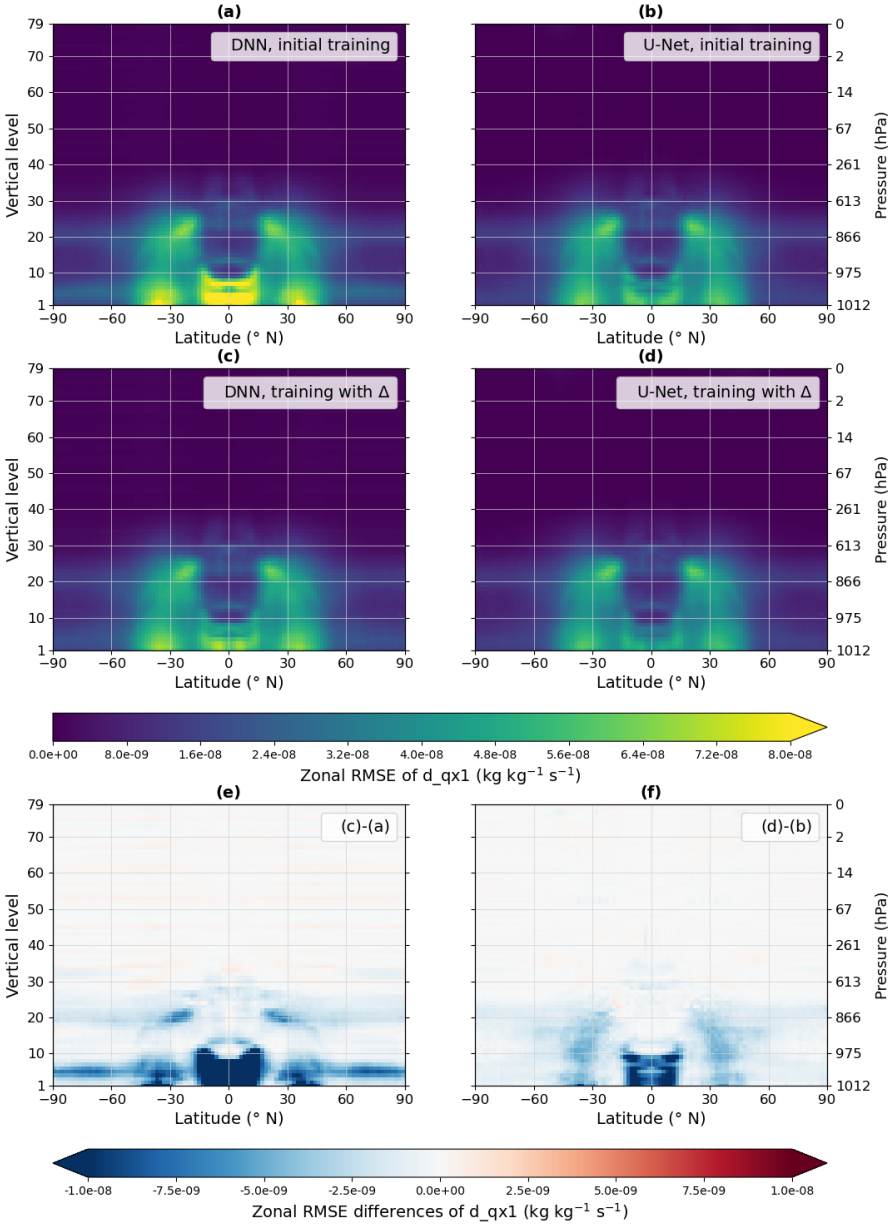

Figure S10. Cross-sections of the zonal RMSE of the humidity tendency *d_qx1* for the test subset. Figures **(a)** and **(b)** show the results from the DNN and the U-Net respectively, from the initial approach in both cases, whereas figures **(c)** and **(d)** are the results of the DNN and the U-Net, with laplacians. Figures **(e)** and **(f)** are respectively the zonal RMSE differences between DNN with laplacians **(c)** and DNN without them **(a)**, and U-Net with laplacians **(d)** and U-Net without them **(b)**.

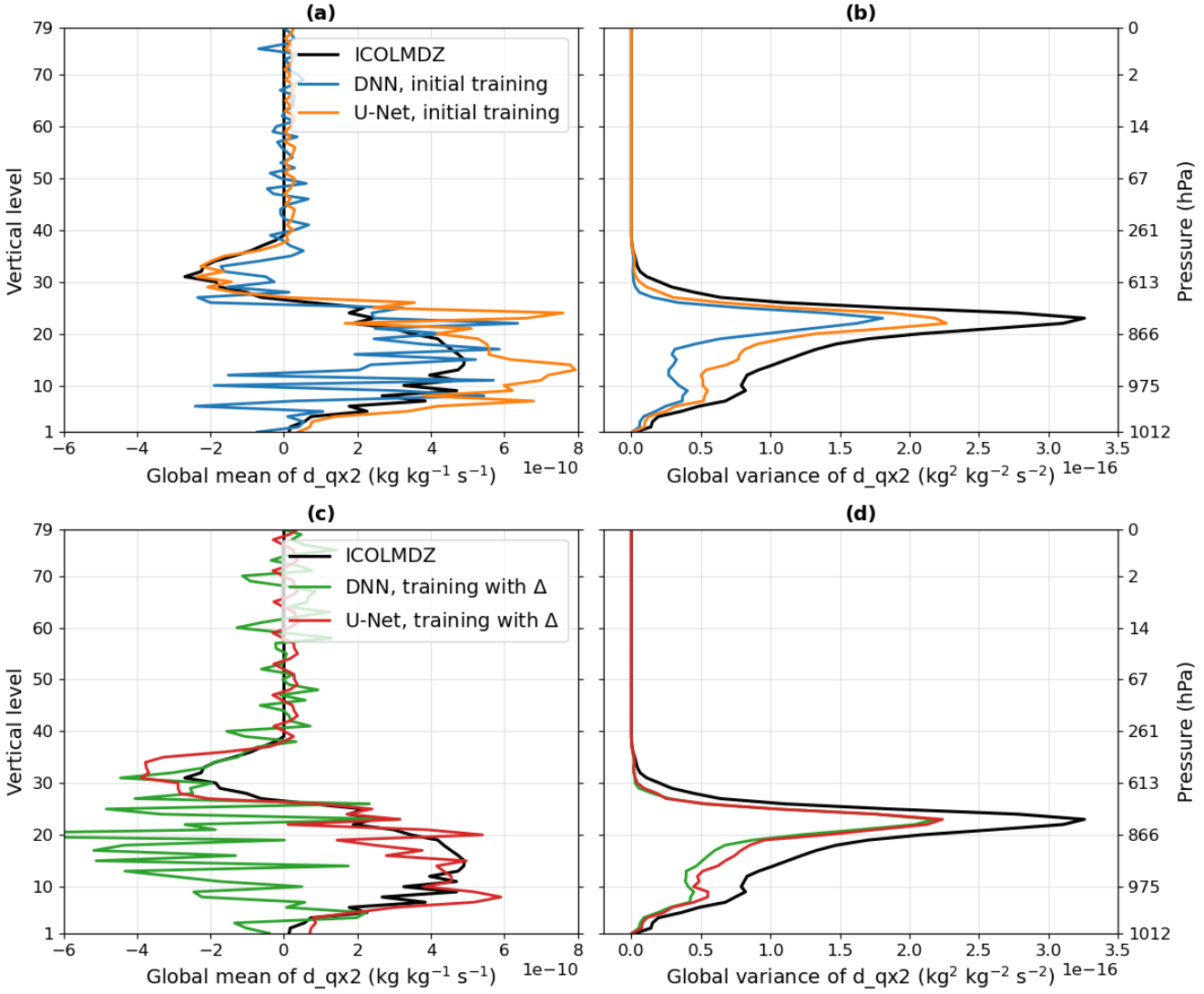

Figure S11. Global vertical profiles of the liquid water tendency *d_qx2* of the mean (left) and the variance (right) for the test subset. Figures **(a)** and **(b)** show the results of the initial training, while figures **(c)** and **(d)** correspond to the second training where physical knowledge is added. In these figures, the black curves represent the real data from the ICOLMDZ simulation. The blue and green curves correspond to predictions made by DNNs while the orange and red curves represent the results obtained using U-Nets.

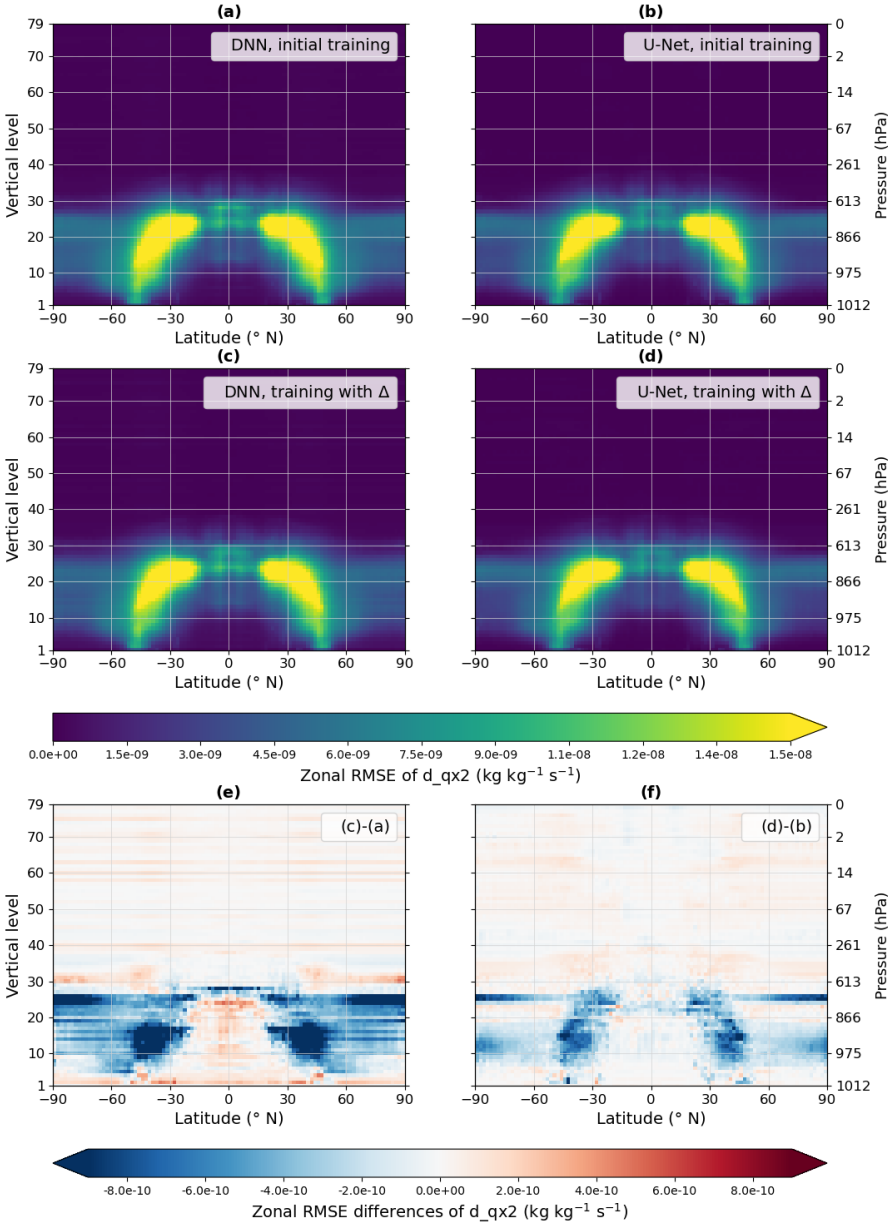

Figure S12. Cross-sections of the zonal RMSE of the liquid water tendency *d_qx2* for the test subset. Figures **(a)** and **(b)** show the results from the DNN and the U-Net respectively, from the initial approach in both cases, whereas figures **(c)** and **(d)** are the results of the DNN and the U-Net, with laplacians. Figures **(e)** and **(f)** are respectively the zonal RMSE differences between DNN with laplacians **(c)** and DNN without them **(a)**, and U-Net with laplacians **(d)** and U-Net without them **(b)**.

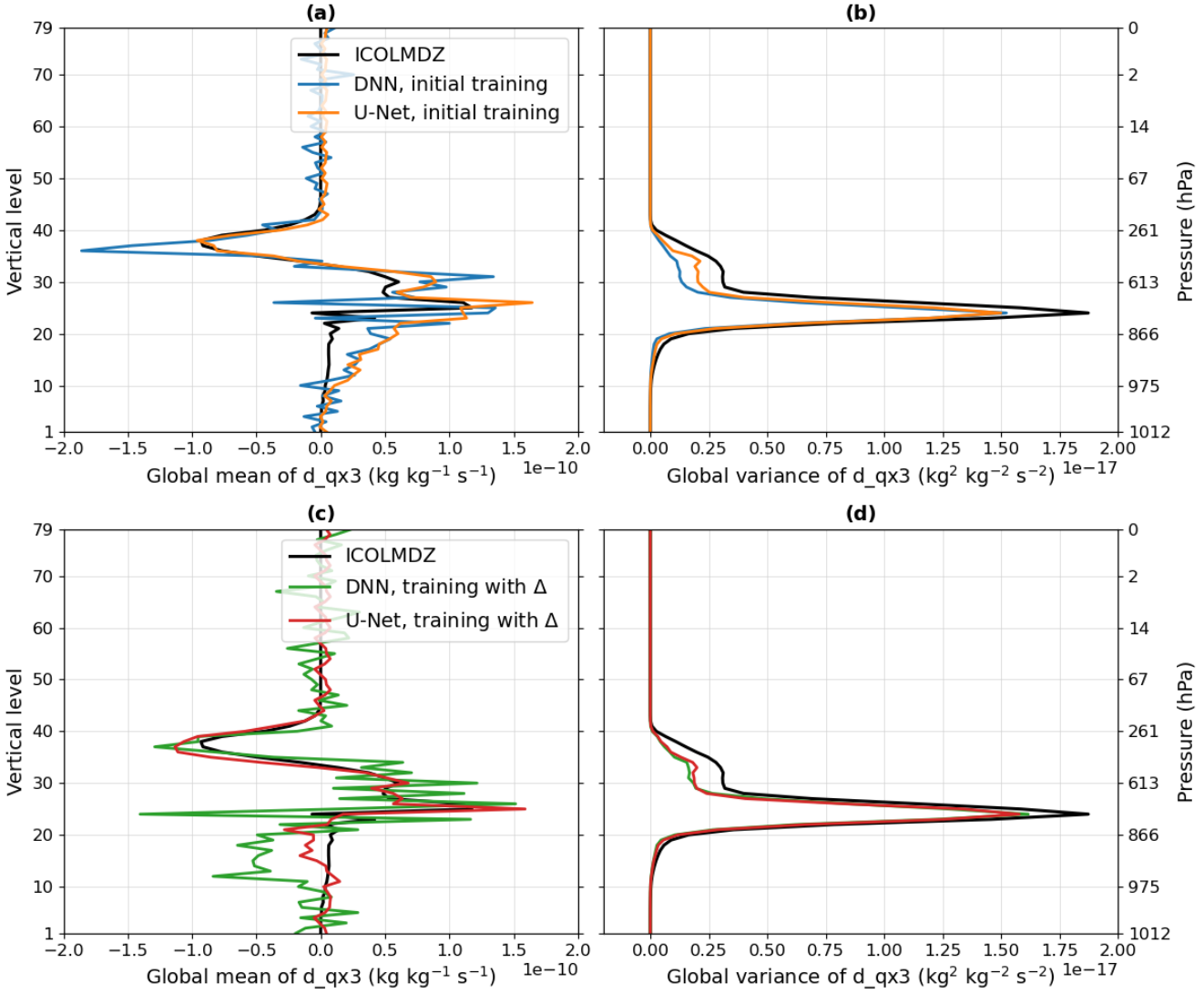

Figure S13. Global vertical profiles of the ice water tendency *d_qx3* of the mean (left) and the variance (right) for the test subset. Figures **(a)** and **(b)** show the results of the initial training, while figures **(c)** and **(d)** correspond to the second training where physical knowledge is added. In these figures, the black curves represent the real data from the ICOLMDZ simulation. The blue and green curves correspond to predictions made by DNNs while the orange and red curves represent the results obtained using U-Nets.

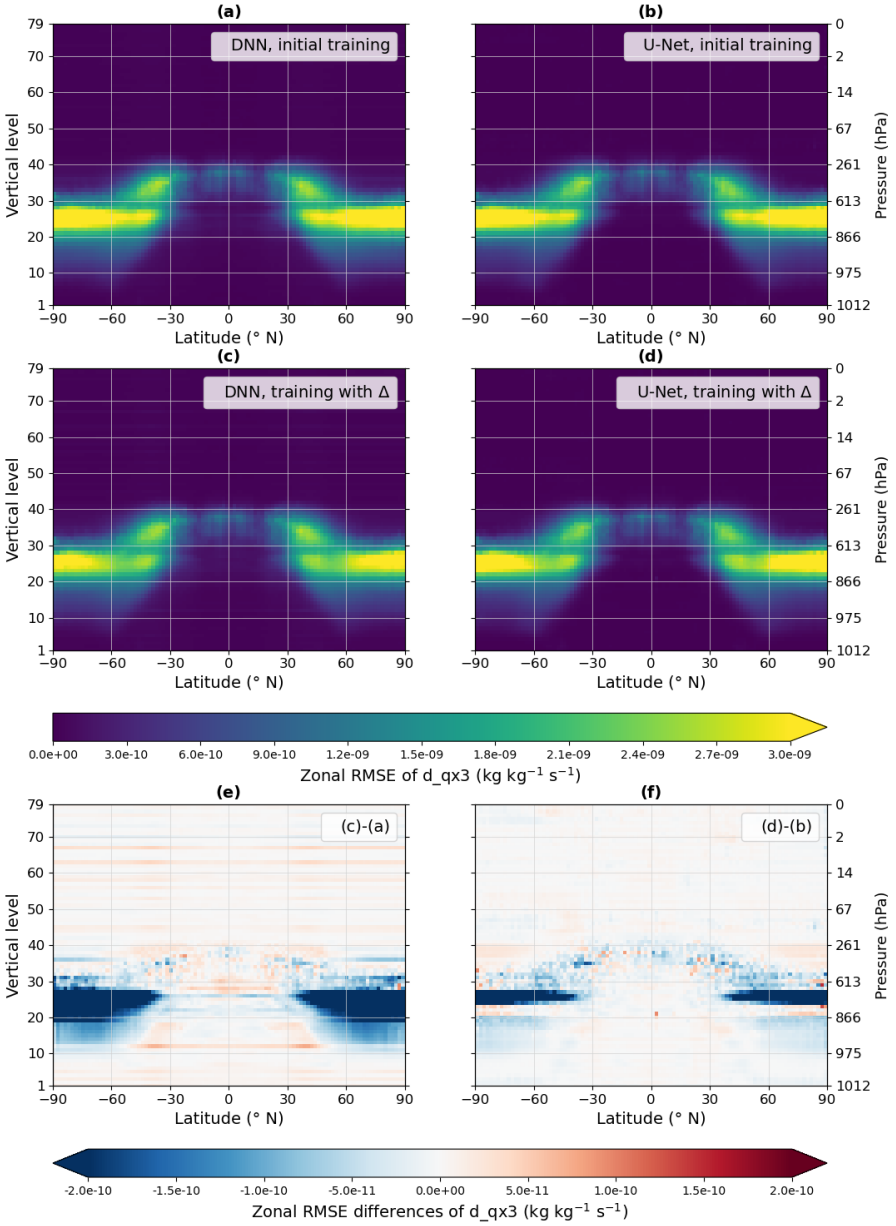

Figure S14. Cross-sections of the zonal RMSE of the solid water tendency *d_qx3* for the test subset. Figures **(a)** and **(b)** show the results from the DNN and the U-Net respectively, from the initial approach in both cases, whereas figures **(c)** and **(d)** are the results of the DNN and the U-Net, with laplacians. Figures **(e)** and **(f)** are respectively the zonal RMSE differences between DNN with laplacians **(c)** and DNN without them **(a)**, and U-Net with laplacians **(d)** and U-Net without them **(b)**.